Suppression of self-discharge in a non-flowing bromine battery via in situ generation of countercharged groups

Wang, Yanfang; Yi, Zhibin; Luo, Wen; Qin, Ning; Luo, Guangfu; Allan, Phoebe K.; Zhang, Fucai; Lu, Zhouguang

DOI:
10.1016/j.xcrp.2021.100620

Cell Reports
Physical Science

CellPress
OPEN ACCESS

Article

Suppression of self-discharge in a non-flowing bromine battery via *in situ* generation of countercharged groups

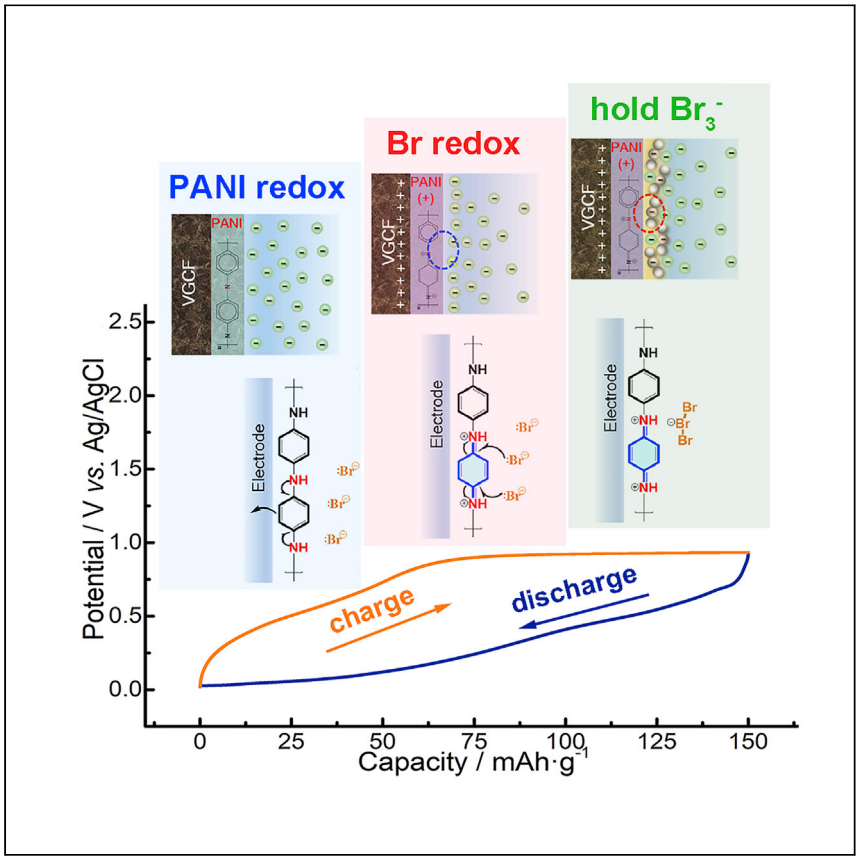

A high Coulombic efficiency is achieved by Wang et al. in a stationary bromine battery by introducing counter-charged groups on the electrode. Mechanistic studies, including *operando* Raman and theoretical calculations, suggest that the counter-charged groups interact with polybromides and suppress their diffusion.

Yanfang Wang, Zhibin Yi, Wen Luo, ..., Phoebe K. Allan, Fucai Zhang, Zhouguang Lu

p.allan@bham.ac.uk (P.K.A.)
luzg@sustech.edu.cn (Z.L.)
zhangfc@sustech.edu.cn (F.Z.)

Highlights

A non-flowing Br battery is demonstrated to deliver reversible capacity

Self-discharge of polybromides is suppressed by counter-charged groups

Possible mechanisms are proposed upon *operando* Raman and DFT calculations

Wang et al., Cell Reports Physical Science *2*, 100620
November 17, 2021 © 2021
https://doi.org/10.1016/j.xcrp.2021.100620

Cell Reports
Physical Science

CellPress
OPEN ACCESS

Article

Suppression of self-discharge in a non-flowing bromine battery via *in situ* generation of countercharged groups

Yanfang Wang,[1,2,3,5] Zhibin Yi,[1,4,5] Wen Luo,[1] Ning Qin,[1] Guangfu Luo,[1,4] Phoebe K. Allan,[2,6,*] Fucai Zhang,[3,*] and Zhouguang Lu[1,*]

SUMMARY

Bromine is attractive for next-generation energy-storage systems because of its high capacity and natural abundance. However, because of issues relating to self-discharging processes, prototypes involving bromide/bromine redox couples are largely limited to the design of flow cells. Here we propose a method to exploit bromine redox chemistry and demonstrate the feasibility of mitigating ion depletion in a stationary device. A cell using polyaniline vapor-grown carbon fiber (PANI-VGCF) as the electrode material exhibits close to 100% Coulombic efficiency at a low current density (50 mA/g). Electrochemical results, *operando* Raman spectroscopy, and theoretical analysis provide clues that the strong interaction between protonated PANI and Br^-/ Br_3^- makes their decoupling unfavorable, thereby suppressing self-discharge processes. This strategy could be utilized for rational design of other conjugated materials/bromine systems without self-discharge issues.

INTRODUCTION

The intermittence of electricity generated by solar panels or wind plants as well as the burgeoning market for electric vehicles requires development of high-performance energy storage systems (ESSs) to better match supply with demand. In recent years, discovering novel materials that could tap into the capacity delivered by anion redox reactions has been regarded as a promising way of developing next-generation ESSs.[1–3] For instance, lithium-rich materials have regained the spotlight over the past decade.[4,5] The contribution of oxygen redox reactions in these materials can deliver higher capacities, but changes in crystal lattices induced by O-O stretching usually lead to inferior cycling stability.[6,7] Another strategy in which anion redox reactions are being used is electrolyte-enhanced supercapacitors and various redox-flow batteries.[8–14] A range of prototypes using oxygen, sulfur, and halogens as redox-active elements to store energy have been proposed for organic and aqueous systems.[15–17] In these systems, capacities are no longer limited by spaces in crystal lattices that cathode materials could provide. Instead, redox couples in the electrolyte determine the majority of the electrochemical properties, meaning that the capacities of such systems can be increased by increasing the concentration or quantity of electrolyte solution.

However, wherever those redox couples are stored, electrochemical reactions take place on the electrode-electrolyte interfaces where electron transfer takes place. Therefore, to achieve high capacity, using flowing catholytes is typical (for example, in Li-I_2, Li-Br_2, or Zn-Br_2 batteries and other systems) to increase the number of

[1]Department of Materials Science and Engineering, Southern University of Science and Technology, Shenzhen 518055, China

[2]School of Chemistry, University of Birmingham, Birmingham B15 2TT, UK

[3]Department of Electronic and Electrical Engineering, Southern University of Science and Technology, Shenzhen 518055, China

[4]Guangdong Provincial Key Laboratory of Computational Science and Material Design, Southern University of Science and Technology, Shenzhen 518055, China

[5]These authors contributed equally

[6]Lead contact

*Correspondence: p.allan@bham.ac.uk (P.K.A.), luzg@sustech.edu.cn (Z.L.), zhangfc@sustech.edu.cn (F.Z.)

https://doi.org/10.1016/j.xcrp.2021.100620

redox-active species in contact with the electrode over a period of time.[18–23] A critical challenge for these systems is the problem of self-discharge, which usually results in low Coulombic efficiency. For instance, upon anodic processes in Br systems, Br^- ions lose electrons to form Br_2 molecules, which then combine with additional Br^- ions in the electrolyte and form polybromides, such as Br_3^- and Br_5^-.[24] Because these species are soluble in the electrolyte, their diffusion from the electrolyte-electrode interface into the bulk electrolyte is thermodynamically favorable, driven by concentration differences. So far, several tactics have been proposed to mitigate self-discharge of Br systems. First, because larger surface areas could provide more sites to accommodate reaction products, porous electrodes have been used widely to increase the liquid-solid interfaces.[25,26] Upon precisely tuning the pore size, some porous carbons could entrap oxidized species and largely prevent self-discharge.[27] Heteroatom doping has also been shown to be effective in increasing adsorption between porous electrode and redox-active species, suppressing their crossover.[28–31]

In this work, we demonstrate a new strategy to mitigate self-discharge in a non-flowing bromine system. Via use of a redox-active polyaniline electrode coating, oppositely charged surface sites are generated *in situ* during the charging process that capture oxidized polybromides on the electrode surface and suppress their diffusion into the electrolyte. This approach results in an impressive Coulombic efficiency of close to 100% when a low current density of 50 mA/g is used. On the basis of electrochemical experiments, *operando* Raman spectroscopy, and theoretical calculations, we propose that the increasing interaction between oxidized polyaniline (PANI) and Br^-/ Br_3^- makes their decoupling difficult, which, in turn, suppresses harmful self-discharge processes.

RESULTS

Preparation and characterization of the PANI-vapor-grown carbon fiber (VGCF)

The PANI-VGCF was prepared via two-step activation of the VGCF and *in situ* polymerization of aniline (see details in the Supplemental experimental procedures). In short, to create a suitable surface for aniline adsorption and its uniform polymerization, the pristine VGCF was first treated by $CuCl_2$ and activated in H_2SO_4, producing materials referred to here as porous VGCF and activated VGCF, respectively. $CuCl_2$ has been shown to be a moderate activation agent to create porous tunnels in biomass materials without destroying their main structures.[32] Acid activation is a widely used method to introduce -OH/-COOH groups on carbon surfaces, helpful for ion/molecule accumulation and crystal nucleation.[33] According to X-ray diffraction (XRD) patterns (Figure 1A), the peak at 26° two-theta (λ = 1.54 Å), corresponding to the (002) plane in graphic matrix, is well maintained after $CuCl_2$ treatment.[34] Gaussian fitting results show that the full width at half maxima (FWHM) of the (002) peak in XRD patterns increases from 0.443(7)° to 0.750(6)° after H_2SO_4 treatment, which, together with the increasing I_D/ I_G ratio in Raman spectra, indicates increased disorder of the graphite structure in the activated VGCF (Figure 1B; Figure S1; Table S1). Scanning electron microscopy (SEM) images reveal that the porous VGCF generally inherits the shape of the pristine VGCF, but some fractures can be seen on its surface, demonstrating $CuCl_2$ etching at high temperature (Figures 1C and 1D). The specific surface area increases from 32.96 m^2/g to 73.68 m^2/g (Figure S2; Table S2). Further acid activation to some extent destroys the original shape of the VGCF, and many cracks appear on the surfaces of carbon fibers (Figure 1E). Polymerization of aniline occurred in a dispersion of the activated VGCF, during which the reaction vessel was cooled in an ice bath, and ammonium persulfate (APS) was

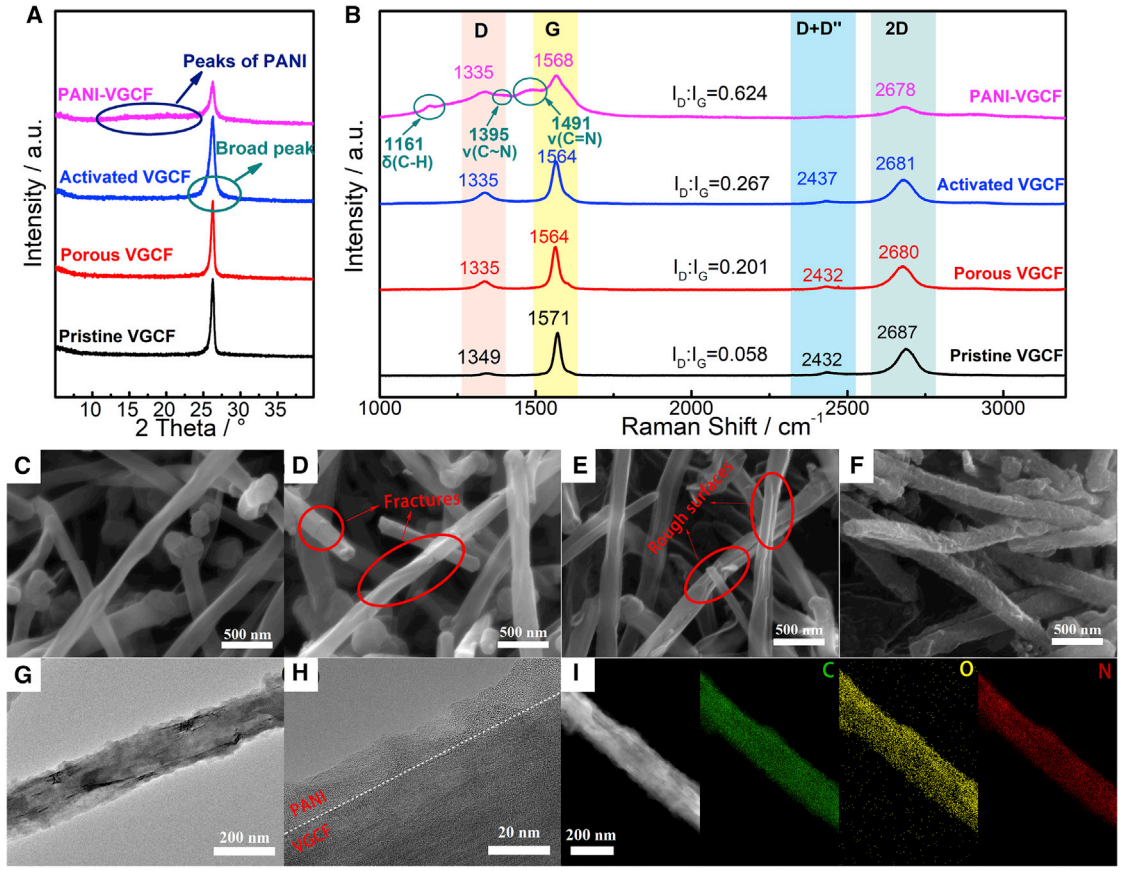

Figure 1. Characterization of the PANI-VGCF

(A) XRD patterns (λ = 1.54 Å) of pristine VGCF, porous VGCF, activated VGCF, and PANI-VGCF.

(B) Raman spectra (monochromatic laser with an excitation line of 532 nm) of pristine VGCF, porous VGCF, activated VGCF, and PANI-VGCF. -, =, and ~ refer to a single bond, a double bond, and a bond intermediate between a single and a double bond, respectively. δ, in-plane bending; ν, in-plane stretching.

(C–F) SEM images of pristine VGCF (C), porous VGCF (D), activated VGCF (E) and PANI-VGCF (F).

(G and H) TEM images of PANI-VGCF.

(I) Energy dispersive X-ray (EDX) mapping of PANI-VGCF.

used as the initiator. As displayed in Figures 1F and 1G, after polymerization, some nanoparticles grow evenly on the surface of the VGCF, forming an outer layer with a thickness of around 10 nm. Although the absence of lattice fringes in the transmission electron microscope (TEM) image indicates its low crystallinity (Figure 1H), we assign the outer layer to PANI from broad peaks between 10°–25° in the XRD patterns.[35] Fourier transform infrared spectroscopy (FTIR) reveals introduction of groups belonging to PANI (Figure S3). Elemental mapping shows uniform distribution of C, O, and N, which are assigned to the VGCF substrate/PANI, -OH/-COOH groups, and PANI, respectively (Figure 1I). Raman spectra further prove successful growth of PANI because new bands appear at 1,161, 1,395, and 1,491 cm^{-1} for the PANI-VGCF, which are at the correct frequency for assignment to C-H in-plane bending, C~N stretching, and C = N stretching relating to quinoid segments, respectively.[36,37]

Electrochemistry of Br-redox on the VGCF electrode

For electrochemistry experiments, a three-electrode system was used in which the active-material loaded carbon rod, a bared carbon rod, and an Ag/AgCl electrode

were connected as the working electrode, the counter electrode, and the reference electrode, respectively. A mixture solution of 0.5 M KBr and 0.25 M K_2SO_4 was used as the electrolyte, and the pH was tuned to 3 because acidic conditions are known to suppress side reactions in Br oxidization and favor reversible conversion between Br^- and Br_2.[38,39] Figure S4 compares cyclic voltammetry (CV) curves of different materials within different potential windows. Generally, for the pristine VGCF electrode, the porous VGCF electrode, and the activated VGCF electrode, rectangular CV curves are observed in the low potential region (<0.8 V), reminiscent of charge storage in electric double layers (EDLs).[40] In the high potential region (>0.8 V), upon charging, the sharp rise of response current relates to oxidation of Br^-, but no peak current is observed because Br^- is in excess in the electrolyte. Upon discharging, the cathodic peaks indicate Br_2/ Br_3^- reduction. Accordingly, a combined mechanism functions in those systems; i.e., physical adsorption of ions in the low potential region and Br redox in the high potential region. Among them, the activated VGCF electrode exhibits the highest response currents, indicating its large surfaces available to store and to hold more reaction products.

Mechanism of evolution of Br-redox chemistry upon introduction of PANI

PANI coating introduces new redox reactions into this system, signified by a pair of broad peaks that appear in the middle potential region for the PANI-VGCF electrode (Figure S4D). As displayed in Scheme S1, via electrochemical reactions or base/acid treatment, PANI interconverts from polyleucoemeraldine (I, reduced state) to polyemeraldine (II, half reduced-half oxidized state) and polypernigraniline (III, oxidized state).[41,42] Removing electrons from I or adding protons to II produces protonated polyemeraldine, among which semiquinone radical (SQR) cation (IV, polaronic type) and quinoid dication (V, bipolaronic type) coexist. Generally, PANI provides capacitances upon reversible transformation between the reduced state and the oxidized state (Scheme S2).[43] The anodic and cathodic peaks of the CV of the PANI-VGCF electrode performed in 1 M H_2SO_4 (i.e., without the presence of Br redox; Figure S5) are assigned to protonation and deprotonation of the PANI, respectively. Therefore, for the PANI-VGCF electrode, EDL capacitance, pseudo-reactions of PANI and Br redox contribute to its capacity.

The charge storage mechanism could be elucidated further by the relationship between the response current (i; mA/g) and the scan rate (v; mV/s) in CV curves, following the equation $i = av^b$, where the b value is 1 for ideal capacitors and 0.5 for Faradic processes.[44] As shown in Figure 2A, CV curves of the PANI-VGCF electrode at various scan rates could be divided into two parts; i.e., the low potential region (<0.9 V), where PANI redox is the major contributor, and the high potential region (>0.9 V), where Br redox is the main contributor. For PANI oxidation (anodic peaks around 0.7 V versus Ag/AgCl), the b value is calculated to be 0.65, indicating that this process is largely diffusion controlled (inset in Figure 2A). However, for Br redox, the current of the reduction peak (around 0.9 V versus Ag/AgCl) barely changes with increasing scan rates, implying that the electrochemical reaction step rather than the mass-transfer process is rate determining in Br_2 reduction. It is commonly believed that Br redox in aqueous (acidic) solutions involves several steps:[45,46] the anodic process,

$$Br^-_{sol} \leftrightarrow Br^-_{ads} \quad \text{(Reaction 1A)}$$

$$Br^-_{ads} \rightarrow Br_{ads} + e^- \quad \text{(Reaction 1B)}$$

$$Br_{ads} + Br^-_{ads} \rightarrow Br_{2,\ sol} + e^- \quad \text{(Reaction 1C)}$$

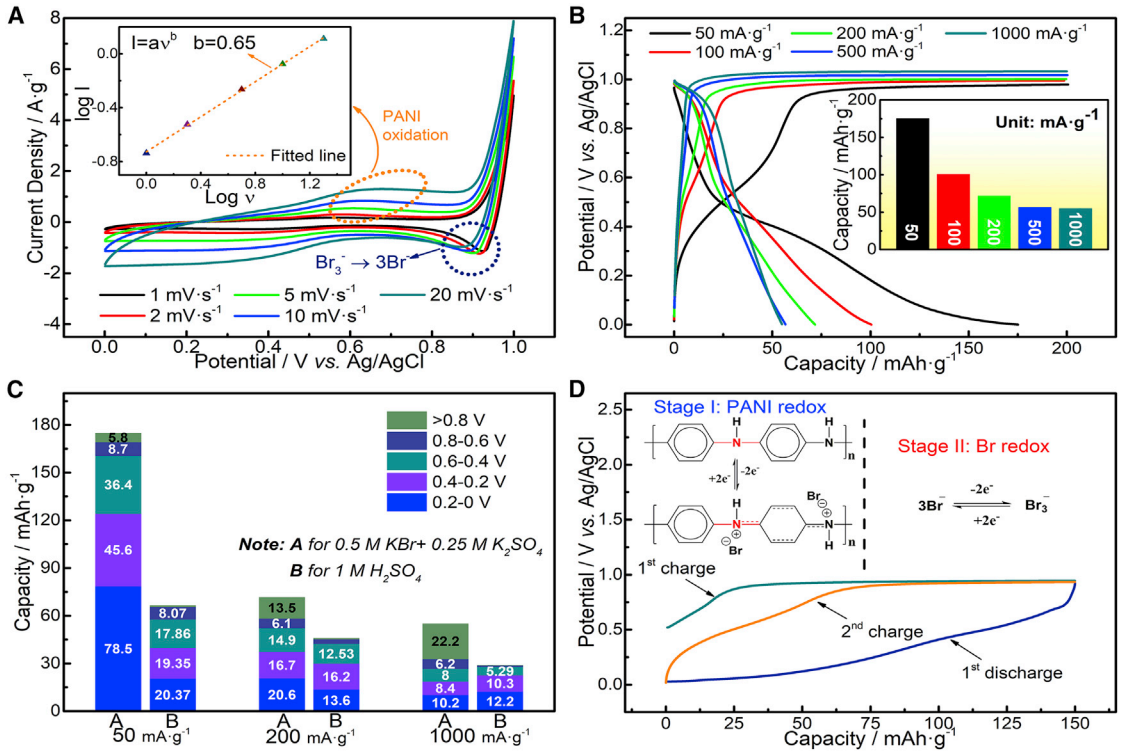

Figure 2. Electrochemistry of the PANI-VGCF electrode

(A) CV curves of PANI-VGCF at various scan rates. Inset: the relationship between response currents and scan rates during PANI oxidization (peaks around 0.7 V versus Ag/AgCl).

(B) Galvanostatic charge-discharge (GCD) curves of PANI-VGCF at different rates. Inset: corresponding discharge capacities.

(C) Divided discharge capacities of PANI-VGCF tested in solution X (0.5 M KBr + 0.25 M K_2SO_4, pH = 3) and solution Y (1 M H_2SO_4).

(D) GCD curves at a fixed capacity of 150 mAh/g. Insets: main reactions that happened in stage I (<0.9 V) and stage II (>0.9 V).

$$Br_{ads} + Br_{ads} \rightarrow Br_{2,\,sol}\,, \qquad \text{(Reaction 1D)}$$

or

and the cathodic process,

$$Br_{2,\,sol} \rightarrow Br_{ads} + Br_{ads} \qquad \text{(Reaction 1E)}$$

$$Br_{2,\,sol} + e^- \rightarrow Br_{ads} + Br^-_{ads} \qquad \text{(Reaction 1F)}$$

or

$$Br_{ads} + e^- \rightarrow Br^-_{ads} \qquad \text{(Reaction 1G)}$$

$$Br^-_{ads} \leftrightarrow Br^-_{sol}\,, \qquad \text{(Reaction 1H)}$$

where the rate-determining step (rds) varies under different conditions. In the anodic process, an ion in solution (Br^-_{sol}) first adsorbs to an active site on the electrode to form a Br^-_{ads} and is oxidized to an adsorbed Br atom (Br_{ads}) along with an electron transfer (Reactions 1A and 1B). In the following formation of a Br_2 molecule ($Br_{2,\ sol}$), the Br_{ads} reacts with a Br^- ion in the solution along with another electron transfer on the same site (Reaction 1C) or combines with a neighboring Br_{ads} (Reaction 1D), depending on the coverage of Br^- and Br_{ads}. Upon discharge, a Br_2 molecule could be reduced to two Br^- ions via reversible reactions, but the rds might be

different; i.e., Reaction 1B is thought to be the rds in the anodic process, and Reactions 1E/1F are regarded as the rds in the cathodic process.

To determine how introduction of PANI affects electrochemical processes, we compare galvanostatic charge-discharge (GCD) performance for the activated VGCF electrode and the PANI-VGCF electrode. Because Br^- is excessive in the electrolyte, all electrodes were charged to a fixed capacity of 200 mAh/g to avoid severe overcharge. The activated VGCF electrode displays a long charge plateau and a sloping discharge plateau, typical for Br^- oxidization and Br_2 reduction, respectively (Figure S6A). In stationary Br batteries, because Br^- is in excess, Br^- ions in the electrolyte could move fast to the electrolyte-electrode interface and compensate consumed ones. Therefore, the potential difference is constant, and a long plateau is typical for Br^- oxidization. However, for Br_2 reduction, the amount of Br_2 diminishes along with discharge, meaning the equilibrium potential changes all the time. Therefore, the discharge curve is in the shape of a slope rather than a plateau. It is noteworthy that its capacity increases from 28.5 mAh/g at the current density of 50 mA/g to 44.9, 51.0, 51.0, and 50.1 mAh/g at 100, 200, 500, and 1,000 mA/g, respectively. The low capacity at 50 mA/g reveals that the activated VGCF fails to retain the oxidized species on the electrode surface, allowing their migration into the bulk electrolyte and causing gradual self-discharge. Such an effect is reduced at high rates because the crossover of charges is kinetically unfavorable within shorter time frames, leading to the unusual rise in capacity. Upon increasing the current density, the charging plateau moves to higher potentials, which, along with the rightward-shifting anodic peaks in its V versus dV/dQ curves (Figure S6B), reveals polarization. Because Br^- is excessive in the solution, the polarization might be caused mainly by the sluggish activity of the rds; i.e., Reaction 1B. On the other hand, the capacity delivered on discharge barely changes when increasing the current density from 100 to 1,000 mAh/g, indicating that the capacity of around 50 mAh/g might be the maximum the activated VGCF electrode could deliver. Despite the stable capacity, its discharge slope moves to lower potentials at higher rates. According to its cathodic V versus dV/dQ curves, the Br_2 reduction peak becomes broader and even splits into two peaks at 1,000 mA/g, which reflects the polarization and offers proof of multi-step electrochemical reactions. Because the electrode is overcharged, Br_2 accumulates in the near-electrode area, and the first reduction step of Reactions 1E/1F is not limited by mass transfer. However, for the following Reaction 1G, its rate is affected by desorption of Br^- produced in Reaction 1F; i.e., it is a diffusion-controlled process. Therefore, upon increasing the current, the cathodic peak at 0.82 V (versus Ag/AgCl) splits into two peaks, representing Reactions 1E/1F and Reaction 1G, respectively. The second peak moves to lower potential because of the sluggish mass transfer. Accordingly, Br redox on the activated VGCF electrode to a great extent follows the mechanisms proposed in Reactions 1A–1H.

For the PANI-VGCF electrode, PANI largely reshapes Br redox chemistry. As shown in Figure 2B, the PANI-VGCF electrode delivers a capacity of 175 mAh/g at a current density of 50 mA/g, which is substantially higher than the capacity it shows in sulfuric acid (66.6 mAh/g at 50 mA/g; Figure S7), indicating that Br^-/ Br_2 redox couples in the electrolyte contribute extra capacity to this system. During the charge process, PANI and Br redox function successively; i.e., oxidization of PANI accounts for the capacity between 0–0.9 V (61.5 mAh/g) and the following plateau above 0.9 V probably represents oxidization from Br^- ions to Br_2 molecules. Such a reaction sequence is supported by theoretical calculations; i.e., removal of an electron from the reduced PANI is more energetically favorable than oxidation of Br^- (see details in

Figure S8). Upon discharge, although high capacity is achieved, introduction of PANI significantly alters the electrochemical performance of Br^-/ Br_2 couples; i.e., the voltage declines rapidly to below 0.6 V. In its V versus dV/dQ curves, the cathodic peak for Reactions 1E/1F disappears (Figure S9). Figure 2C compares divided discharge capacities in different potential regions of the PANI-VGCF electrode in H_2SO_4 solution and Br-containing electrolyte. Of the region above 0.8 V, it shows the capacity of 5.8 and 0.95 mAh/g in Br-containing electrolyte and H_2SO_4 solution, respectively. The increase in capacity reveals that some Br_2 molecules are reduced similar to those on the activated VGCF electrode. However, it only accounts for 3.3% of the total capacity. The most significant increase in capacity is observed at voltages of less than 0.6 V; (i.e., after the PANI has been partially reduced [<0.6 V]), indicating that the major reduction of Br_2 proceeds in parallel with further PANI reduction.

In acidic solutions, a Br_2 molecule usually combines with a Br^- ion and exists in the form of $Br_{3,\ sol}^-$ (Reaction 1I), which adsorbs to the positively charged electrode via physisorption or electro-adsorption.[47] For the PANI-VGCF electrode, positive charge centers in protonated PANI (N_{PANI}^+) are ideal sites to capture $Br_{3,\ sol}^-$, resulting in stronger interaction between $Br_{3,\ sol}^-$ and N_{PANI}^+ (Reaction 1J):[48]

$$Br_{2,\ sol} + Br_{sol}^- \leftrightarrow Br_{3,\ sol}^- \qquad \text{(Reaction 1I)}$$

$$Br_{3,\ sol}^- + N_{PANI}^+ \leftrightarrow Br_{3,\ ads}^- - N_{PANI}^+ . \qquad \text{(Reaction 1J)}$$

At this point, desorption of Br_3^- or decoupling of $Br_{3,\ ads}^- - N_{PANI}^+$ needs to overcome a high energy penalty, causing large electrochemical polarization. Increases in internal resistance (Re) and charge transfer resistance (Rct) after PANI coating also contribute to such high overpotentials between charge and discharge curves (Figure S10). Upon increasing the current density, the capacity decreases to 100.5, 71.8, 56.7, and 55.0 mAh/g at 100, 200, 500, and 1,000 mA/g, respectively. Interestingly, its discharge slope moves upward to higher potentials, indicating that the effect of PANI on tuning Br redox chemistry is weakened. Because the amount of Br_3^- the PANI adsorbs is basically determined by the number of N_{PANI}^+ sites, the sluggish PANI oxidation reaction at high rates leads to increasing Br_2 reduction following traditional pathways. Therefore, the cathodic peak in V versus dV/dQ curves reappears and increases at high rates, which is consistent with the trend depicted in Figure 2C and Table S3. When charged to a fixed capacity of 150 mAh/g at a low current density of 50 mAh/g, the PANI-VGCF electrode delivers a Coulombic efficiency of close to 100%, which we assign to reactions of PANI in stage I and Br redox in stage II (Figure 2D). The PANI-VGCF electrode presents Coulombic efficiencies of higher than 99% with 6 h relaxation between charge and discharge processes, meaning the self-discharge is largely suppressed (Figure S11).

Cycling performance of the PANI-VGCF electrode

Upon further cycling, although the PANI-VGCF electrode exhibits good capacity retention for 50 cycles, the capacity contributed by PANI redox fades gradually (Figure S12). The shrinking amount of protonated PANI has knockon effects for Br redox chemistry; its effect on reshaping Br redox chemistry is largely diluted, which accounts for the reappearance of Br_2 reduction peaks at around 0.9 V in the cathodic V versus dV/dQ curves (Figure S13). Gradual depletion of PANI is supported by the decreasing intensity of Raman bands attributed to PANI and the appearance of bared surfaces on VGCF, as observed in SEM images (Figures S14 and S15). Notably, energy-dispersive X-ray (EDX) mapping results reveal that C, O, and N no longer distribute uniformly; i.e., N accumulates in areas with PANI coating (Figure S16).

Moreover, the cycled sample contains 1.01% Br (atomic fraction), probably resulting from bromination of PANI. Details about bromination are presented in Scheme S3 and discussed in Note S1. From this perspective, although self-discharge of Br_2/Br_3^- is largely mitigated by introducing PANI redox, entangling Br redox into PANI deteriorates its long-term stability, which should be the subject of further studies.

Probing structural changes of the PANI-VGCF electrode by *operando* Raman spectroscopy

Given that chemical changes are always accompanied by geometric reconstructions, Raman spectroscopy is sensitive to evolution of PANI structure during redox reactions. Figure S17 displays Raman spectra of the pristine PANI-VGCF electrode and its various components. It is noteworthy that the red excitation line (785 nm) gives richer spectra than the green line (532 nm; Figure 1B), probably resulting from the selective resonant enhancements of benzenoid or quinoid rings.[49] Detailed assignments of Raman bands are listed in Table S4 and explained in Note S2.

The proposed mechanism for the PANI-VGCF electrode was probed further using *operando* surface-enhanced Raman scattering (SERS) spectroscopy experiments. To record the full process of PANI redox, the second cycle was chosen for the *operando* Raman study (Figures 3A and 3B). The sensitivity of the 785-nm laser to the resonant effects of quinoid segments (e.g., the bands of C-N-C torsion [450 cm^{-1}], C-H in-plane bending [1,170 cm^{-1}], C∼N stretching [1,300–1,400 cm^{-1}], and C = N stretching [1,500 cm^{-1}]) allows us to use these bands as indicators for PANI oxidization.[50,51] The rise of their intensity upon charging from 0.02 to 0.90 V indicates the increasing amount of quinoid segments (Figure 3C; Figure S18) during these electrochemical processes. Hence, PANI oxidization contributes to the charge capacity during this process, which is consistent with its established electrochemical properties.[35] However, upon further charging to above 0.9 V, the intensity of these bands declines dramatically, revealing that involvement of Br redox intensively reconstructs the electronic structure of oxidized PANI and that the conjugating polymer presents more benzenoid features.

For the oxidized PANI, no matter whether it is in in the form of polaron or bipolaron, counterions or dopants (i.e., Br^- in this case) spontaneously transfer to the N^+_{PANI} sites because of electrostatic adsorption. According to Reaction 1B, the adsorbed Br^-_{ads} will lose an electron to form a Br_{ads} atom/radical, which then forms Br_2/Br_3^- and exists as $Br^-_{3,\ ads} - N^+_{PANI}$. Nevertheless, a stronger interaction means that the decoupling of $Br^-_{3,\ ads} - N^+_{PANI}$ requires higher energy. Therefore, when discharging, the voltage drops quickly to below 0.6 V, whereas Raman bands representing quinoid rings are still ambiguous, indicating that the interaction between PANI and Br remains. Upon further discharge, quinoid-related Raman bands reappear, barely decay until 0.08 V, and finally disappear in the fully discharged state at 0.03 V. From this aspect, although Br redox reshapes the electronic structure of oxidized PANI, the PANI-VGCF electrode undergoes reversible changes because its Raman spectra are restored by the end of the discharge. To understand how Br redox induces electronic reconstruction on oxidized PANI, we investigated the evolution of Raman bands relating to C-N-C segments because Br^- ions are likely to remain on the protonated N^+_{PANI} sites, and their oxidization could directly affect the adjacent C-N-C segments (Figure S19). Figures 3D–3H depict possible evolutions of Br-PANI interactions along with their Raman spectra at different voltages. The band at around 521 cm^{-1} could be assigned to C-H wagging and C-N^+ = C torsion in quinoid

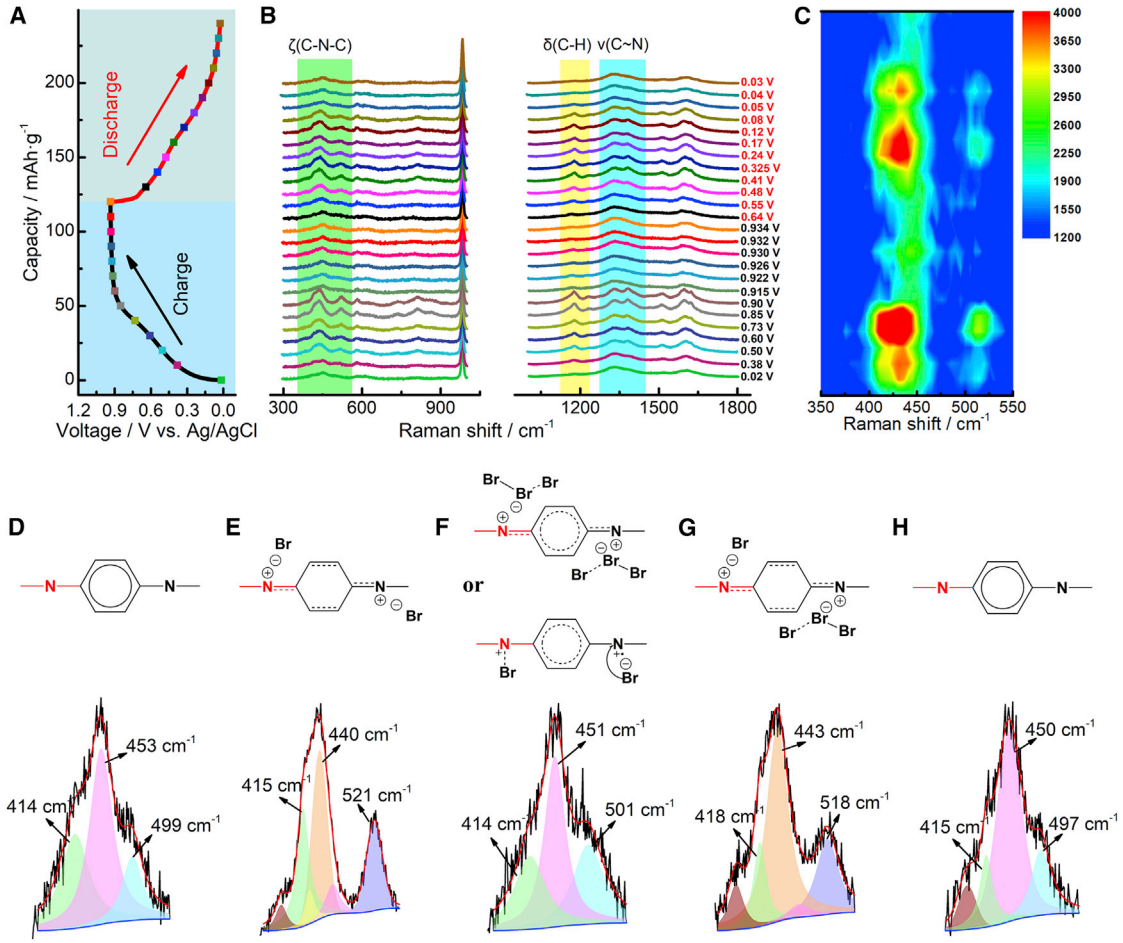

Figure 3. *Operando* Raman spectroscopy of the PANI-VGCF electrode

(A) Second GCD curves of the *in situ* cell.

(B) *Operando* SERS spectra collected by using the 785-nm laser. Shaded areas highlight stretches of interest: ν, in-plane stretching (blue); ζ, out-of-plane torsion (green); δ. in-plane bending (yellow).

(C) Contour map for Raman bands relating to C-N-C torsion and C-H wagging.

(D–H) Evolution of benzenoid/quinoid segments and their Raman spectra at C-0.02 V (D), C-0.9 V (E), C-0.934 V (F), D-0.48 V (G) and D-0.03 V (H). C and D refer to charge process and discharge process, respectively. Bands at around 521 and 453 cm^{-1} could be assigned to C-H out-of-plane wagging and torsions of C-N-C segments (red parts).

segments,[52,53] whose disappearance in the fully charged state (0.934 V) also proves that the π-conjugated network is reconstructed significantly during Br redox.

Theoretical structure and Raman evolutions

Density-functional theory (DFT) calculations were carried out to probe the reconstruction of electronic structures and the Raman changes during (dis)charge (see details in the Supplemental experimental procedures). As shown in Figures S20A–S20C, upon oxidization of PANI, the benzene ring distorts asymmetrically and two adjacent C-C bonds stretch inversely (i.e., one becomes shorter and another becomes longer), corresponding to the benzenoid-to-quinoid evolution. Consequently, new Raman bands relating to C-N^+~C torsion ($\zeta(C\text{-}N^+\sim C)_{SQR}$), C~N stretching ($\nu(C\sim N^+)_Q$), and C-C ($\nu(C\text{-}C)_Q$) stretching vibrations emerge in the theoretical Raman spectra (Figure S20D). Such an asymmetrical evolution is enhanced by Br^- adsorption, and the electron cloud condenses further at the short C-C bond, resulting in increasing Raman signals for $\zeta(C\text{-}N^+ = C)_Q$ and $\zeta(C\text{-}N^+\sim C)_{SQR}$

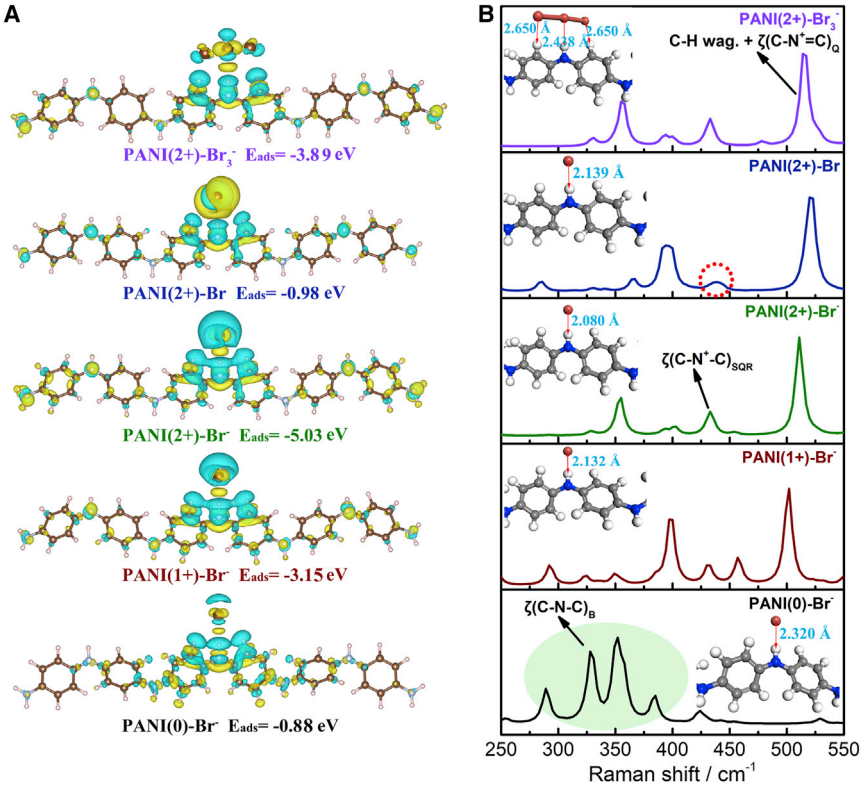

Figure 4. Theoretical structure and Raman evolutions

(A) Differential charge densities and calculated adsorption energies of PANI(0)-Br^-, PANI(1+)-Br^-, PANI(2+)-Br^-, PANI(2+)-Br, and PANI(2+)-Br_3^-. The charge density isosurfaces are 0.001 e/bohr^3 for blue and −0.001 e/bohr^3 for yellow.

(B) Theoretical Raman spectra for PANI(0)-Br^-, PANI(1+)-Br^-, PANI(2+)-Br^-, PANI(2+)-Br, and PANI(2+)-Br_3^-. Insets: the distances between Br and PANI in optimized structures.

(Figure S21). A segment of six hexagonal carbon rings was used as the local structure to study electron density changes along with ion adsorption (Figure 4A). Upon the removal of 1 and 2 electrons from the reduced PANI segment (PANI(0)), the distance between the Br^- ion and the protonated nitrogen site on PANI reduces from 2.32(0) to 2.13(2) and 2.08(0) Å, corresponding to decreasing adsorption energies from −0.88 to −3.15 and −5.03 eV for PANI(0), PANI(1+), and PANI(2+), respectively. The differential charge density distribution indicates stronger interactions between oxidized PANI and Br^-/ Br_3^- ions, which means that depletion of Br^-/ Br_3^- ions from the PANI electrode is more thermodynamically unfavorable. Because the oxidized PANI has a stronger ability to adsorb Br^-/ Br_3^- ions, self-discharge is largely suppressed in this system.

Although changing the adsorption ions from Br^- to Br_3^- or Br_5^- induces structural changes of the oxidized PANI, its theoretical Raman spectra do not present an obvious quinoid-to-benzenoid transition, contradictory to the experimental results (Figure S22). From this perspective, the rapid quinoid-to-benzenoid transition triggered by Br redox in *operando* Raman spectroscopy could not be assigned solely to the electrostatic adsorption between protonated PANI and counterions. During Br redox, a Br^- ion first becomes a Br atom/radical by losing an electron, which thereafter bonds to another Br atom/radical to form a Br_2 molecule or attacks the SQR to produce an intermediate, as depicted in Figure 3F (denoted as

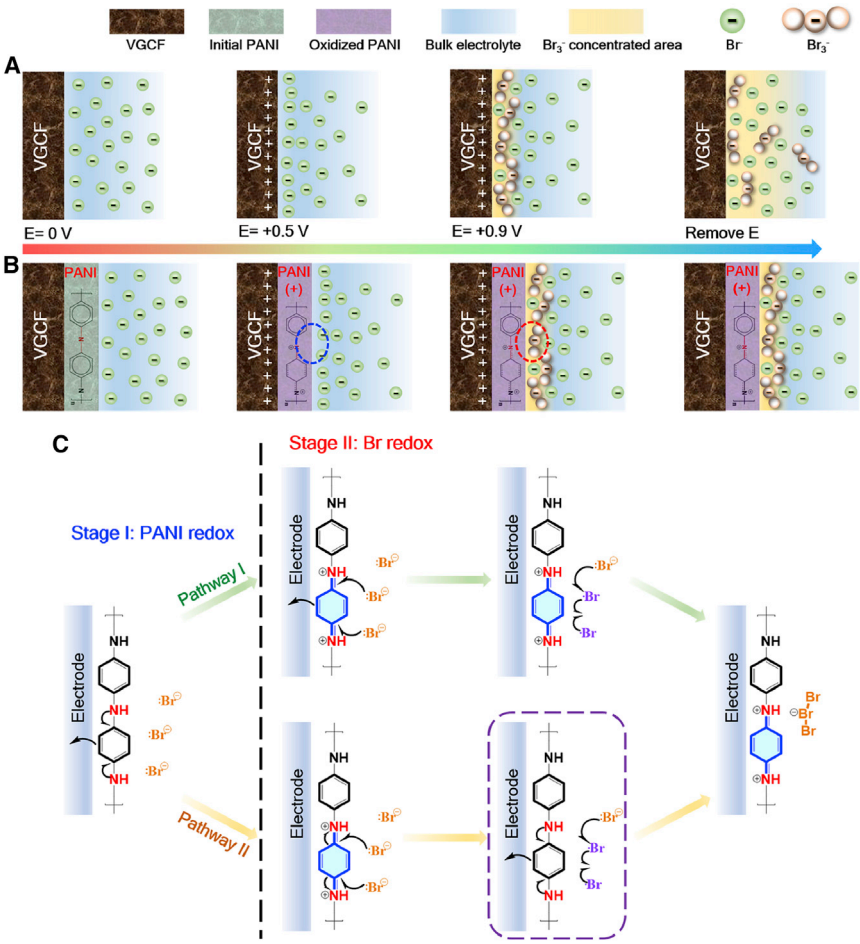

Figure 5. Illustrations of reaction mechanisms

(A and B) Schematic evolutions of the electrode-electrolyte interfaces of the VGCF electrode (A) and the PANI-VGCF electrode (B) upon charging.

(C) Reaction pathways on the PANI-VGCF electrode. Black arrows represent electron transfers.

PANI(2+)-Br). Consequently, the theoretical Raman band belonging to $\zeta(C\text{-}N^{+}\text{-}C)_{SQR}$ largely decreases when Br^{-} is oxidized to a Br atom/radical, which accounts for its decline in *operando* Raman spectra (Figure 4B; Figure S22E).

DISCUSSION

Bromine is attractive for high-capacity energy storage devices, but the self-discharge problem hinders its wide application. As illustrated in Figure 5A, for traditional electrodes (e.g., VGCF), polybromides produced on the electrode-electrolyte interfaces gradually diffuse into the bulk electrolyte after removal of external voltage (E), resulting in low Coulombic efficiencies. To minimize the negative effects of self-discharge, many prototypes adopt flowing designs where external forces are used to circulate bromides/polybromides.[9,10] However, they are only suitable for application scenarios with little concern regarding volumetric energy densities because flowing electrolytes have to be stored in large tanks. Their properties largely rely on the selectivity and endurance of ion-exchange membranes, which play pivotal roles in preventing crossover of bromides/polybromides.[24] Generally, in redox flow batteries, although the self-discharge problem is mitigated in terms of mass

transfer kinetics, diffusion of polybromides from the electrode-electrolyte interfaces into the bulk electrolytes continues to be thermodynamically favorable, meaning that self-discharge is still inevitable in those systems.

Here, to solve this problem, we propose a new strategy of introducing countercharged groups to capture polybromides. When using PANI-VGCF as the electrode material, the oxidized PANI could interact with polybromides after removal of external voltage, retaining them on the electrode-electrolyte interfaces (Figure 5B). On the basis of careful investigation, we propose possible reaction pathways in Figure 5C. Upon charging, the PANI loses electrons and is oxidized in stage I, resulting in benzenoid-to-quinonoid transformation. Further removing electrons from Br^- ions follows two possible pathways: electrons transfer to the VGCF immediately (pathway I) or first hop onto the PANI chain (pathway II). Because VGCF is coated by oxidized PANI, electrons removed from Br^- ions are more likely to transfer to the conductive polymer and induce its reverse quinoid-to-benzenoid transformation (Figure 5C, dashed box), which is supported by *operando* Raman spectroscopy results and theoretical calculations. At present, we still lack knowledge of the exact intermediate formed between oxidize PANI and Br radicals, which requires further work to elucidate. The concept of introducing countercharged groups to retain polybromides should be applicable to a range of p-type organic electrode materials whose redox reactions occur between neutral states and positively charged states.[54] Given the abundance of organic materials, this tactic could bring new opportunities for building Br batteries.

We propose an approach to suppress self-discharge in a stationary Br redox system. For the PANI-VGCF electrode, a high capacity (150 mAh/g) and nearly 100% Coulombic efficiency were achieved at a low current density (50 mA/g). Mechanistic studies reveal that the intermediate (Br atom/radical) and Br_3^- in Br redox could interact with the protonated PANI and reconstruct the electronic structure of the PANI, leading to stronger electrode-electrolyte interactions inhibiting their separation. This work provides an effective strategy to reduce unfavorable self-discharge and opens up possibilities for designing efficient electrodes to take advantage of bromine redox chemistry.

EXPERIMENTAL PROCEDURES

Resource availability

Lead contact

Further information and requests for resources should be directed to and will be fulfilled by the lead contact, Phoebe Allan (P.Allan@bham.ac.uk).

Materials availability

This study did not generate new unique reagents.

Data and code availability

All data needed to evaluate the conclusions in the paper are present in the paper or the Supplemental information.

Materials preparation

Pristine VGCF was purchased and used without further treatment (Showa Denko, Japan). For $CuCl_2$ treatment, pristine VGCF and anhydrous $CuCl_2$ were mixed at a weight ratio of 10:1, ground in a mortar by hand for 0.5 h, and transferred to a tube furnace. The mixture was heated up to 900°C (5°C/min) and annealed for 12 h under argon flow. During this process, the $CuCl_2$ reacted with the graphic matrix

and was partially reduced to Cu metal; defects were supposed to be created on the surface of the pristine VGCF. The product was washed with 1 M HCl under ultrasonication to fully remove residual Cu, rinsed with deionized (DI) water to until the pH was neutral, collected via vacuum filtration, dried in a vacuum oven overnight to remove water (120°C, 24 h), and denoted porous VGCF. For acid treatment, porous VGCF was dispersed in concentrated sulfuric acid (18 M H_2SO_4) with stirring for 3 h. The reaction solution was diluted and filtered under a vacuum. The collected sample was washed thoroughly with DI water, dried in a vacuum oven (120°C, 24 h), and denoted as activated VGCF. For growth of PANI, activated VGCF and aniline monomers were dispersed ultrasonically in 1 M HCl and put in an ice bath (0°C–4°C). Polymerization was triggered by adding APS drop by drop, and the mixed solution was being for 1 h in an ice bath and left in a refrigerator for 24 h (0°C–4°C). The final product of PANI-VGCF was collected by filtering the solution, washing thoroughly with DI water, and drying under a vacuum (80°C, 24 h). See Supplemental experimental procedures for additional details regarding characterization.

Operando Raman measurements

For *operando* Raman testing, a specially designed *in situ* cell was used (Figure S23). The cell had a platinum plate as the current collector for the working electrode, a platinum wire as the counter electrode, and the Ag/AgCl reference electrode. In a real test, one piece of the PANI-VGCF electrode was pressed on the platinum plate, and a paralleling quartz window was used to cover the electrode and seal the *in situ* cell. Because the quartz window is transparent to visible light and Raman inactive, reliable Raman spectra could be collected in reflection mode. To get high-quality Raman spectra, gold nanoparticles were dispersed in ethanol and dropped uniformly on the surface of the electrode before cell assembly. Because of their effects on resonance enhancement, SERS spectra were collected successfully. The corresponding electrochemical performance of the *in situ* cell was recorded using a battery tester (Nova).

First-principles computational details

The Gaussian 16 package was used to perform all calculations.[55] To simplify the modeling, PANI segments with six hexagonal carbon rings were used to modify the structures in various oxidized states and local environments. The geometry of a PANI segment was optimized by the B3LYP functional, and the 6-311G basis set was adopted for further accuracy improvement. Frequency analyses were done with the same basic set to confirm the stability of the optimized structures. When optimization of the geometry was completed, Raman spectra were obtained via GaussView 6.1. Each Raman band was broadened to a Lorentzian line shape with a 4 cm^{-1} line width. Because first-principles calculations were carried out under the assumption that the PANI segments were isolated, their theoretical Raman spectra show differences from experimental data in terms of intensity and band position.

The adsorption energy (E_{ads}) of Br, Br^-, and Br_3^- species (denoted Br*) on PANI (0), PANI (1+), and PANI (2+) segments (denoted PANI*) was calculated by $E_{ads} = E_{PANI*+Br*} - (E_{PANI*} + E_{Br*})$, where $E_{PANI*+Br*}$, E_{PANI*}, and E_{Br*} are the total energies of the whole adsorbed system and isolated PANI* and Br* molecules, respectively. The bonding nature between the PANI* and Br* was investigated by computing the differential charge density from $\Delta\rho = \rho(PANI* + Br*) - \rho(PANI*) - \rho(Br*)$, where $\rho(PANI* + Br*)$, $\rho(PANI*)$ and $\rho(Br*)$ are the total electron charge density of the adsorbed system and isolated PANI* and Br* molecules, respectively. Yellow and blue colors represents charge depletion and accumulation, respectively.

SUPPLEMENTAL INFORMATION

Supplemental information can be found online at https://doi.org/10.1016/j.xcrp.2021.100620.

ACKNOWLEDGMENTS

This work was financially supported by the Basic Research Project of the Science and Technology Innovation Commission of Shenzhen (JCYJ20200109141640095), the Guangdong Innovative and Entrepreneurial Research Team Program (2016ZT06G587), the Guangdong Provincial Key Laboratory of Computational Science and Material Design (2019B030301001), the Introduced Innovative R&D Team of Guangdong (2017ZT07C062), and the National Natural Science Foundation of China (21875097). Help with SEM, Raman, EPR, and XRD characterization from the Core Research Facilities and with DFT simulations from the Center for Computational Science and Engineering at Southern University of Science and Technology is gratefully appreciated.

AUTHOR CONTRIBUTIONS

Y.W. conceived the idea for this study. Y.W. carried out materials preparation and characterization. Y.W. and W.L. performed *operando* Raman testing. Z.Y., Y.W., and G.L. designed theoretical models and performed DFT calculations. Y.W., Z.Y., P.A., and Z.L. drafted the manuscript. All authors participated in discussions of the results as well as revision of the manuscript.

DECLARATION OF INTEREST

The authors declare no competing interests.

Received: July 30, 2021
Revised: September 6, 2021
Accepted: October 1, 2021
Published: October 20, 2021

REFERENCES

1. Larcher, D., and Tarascon, J.-M. (2015). Towards greener and more sustainable batteries for electrical energy storage. Nat. Chem. *7*, 19–29.

2. Kwade, A., Haselrieder, W., Leithoff, R., Modlinger, A., Dietrich, F., and Droeder, K. (2018). Current status and challenges for automotive battery production technologies. Nat. Energy *3*, 290–300.

3. Chu, S., Cui, Y., and Liu, N. (2016). The path towards sustainable energy. Nat. Mater. *16*, 16–22.

4. Xie, Y., Saubanère, M., and Doublet, M.-L. (2017). Requirements for reversible extra-capacity in Li-rich layered oxides for Li-ion batteries. Energy Environ. Sci. *10*, 266–274.

5. Ben Yahia, M., Vergnet, J., Saubanère, M., and Doublet, M.-L. (2019). Unified picture of anionic redox in Li/Na-ion batteries. Nat. Mater. *18*, 496–502.

6. Sathiya, M., Abakumov, A.M., Foix, D., Rousse, G., Ramesha, K., Saubanère, M., Doublet, M.-L., Vezin, H., Laisa, C.P., Prakash, A.S., et al. (2015). Origin of voltage decay in high-capacity layered oxide electrodes. Nat. Mater. *14*, 230–238.

7. Chen, C.J., Pang, W.K., Mori, T., Peterson, V.K., Sharma, N., Lee, P.H., Wu, S.H., Wang, C.C., Song, Y.F., and Liu, R.S. (2016). The Origin of Capacity Fade in the Li2MnO3·LiMO2 (M = Li, Ni, Co, Mn) Microsphere Positive Electrode: An Operando Neutron Diffraction and Transmission X-ray Microscopy Study. J. Am. Chem. Soc. *138*, 8824–8833.

8. Li, C.H., Yoshida, Y., Date, R., Matsushita, K., Ishii, Y., and Kawasaki, S. (2018). Bromine aqueous electrolyte redox capacitor using carbon nanotubes. Mater. Express *8*, 555–561.

9. Liu, W., Liu, Y., Zhang, H., Xie, C., Shi, L., Zhou, Y.G., and Li, X. (2019). A highly stable neutral viologen/bromine aqueous flow battery with high energy and power density. Chem. Commun. (Camb.) *55*, 4801–4804.

10. Zeng, Y.K., Yang, Z.F., Lu, F., and Xie, Y.L. (2019). A novel tin-bromine redox flow battery for large-scale energy storage. Appl. Energy *255*, 113756.

11. Hu, B., DeBruler, C., Rhodes, Z., and Liu, T.L. (2017). Long-cycling aqueous organic redox flow battery (AORFB) toward sustainable and safe energy storage. J. Am. Chem. Soc. *139*, 1207–1214.

12. Frackowiak, E., Meller, M., Menzel, J., Gastol, D., and Fic, K. (2014). Redox-active electrolyte for supercapacitor application. Faraday Discuss. *172*, 179–198.

13. Lota, G., and Frackowiak, E. (2009). Striking capacitance of carbon/ iodide interface. Electrochem. Commun. *11*, 87–90.

14. Chun, S.E., Evanko, B., Wang, X., Vonlanthen, D., Ji, X., Stucky, G.D., and Boettcher, S.W. (2015). Design of aqueous redox-enhanced electrochemical capacitors with high specific energies and slow self-discharge. Nat. Commun. *6*, 7818.

15. Wang, L.N., Wang, X.F., Liu, J.Y., Yang, H., Fu, C.M., Xia, Y.Y., and Liu, T.X. (2018). A rechargeable metal-free full-liquid sulfur-bromine battery for sustainable energy storage. J. Mater. Chem. A Mater. Energy Sustain. *6*, 20737–20745.

16. Yu, F., Zhang, C.M., Wang, F.X., Gu, Y.Y., Zhang, P.P., Waclawik, E.R., Du, A.J., Ostrikov, K., and Wang, H.X. (2020). A zinc bromine

"supercapattery" system combining triple functions of capacitive, pseudocapacitive and battery-type charge storage. Mater. Horiz. *7*, 495–503.

17. Zhao, X., Zhao-Karger, Z., Fichtner, M., and Shen, X. (2020). Halide-based materials and chemistry for rechargeable batteries. Angew. Chem. Int. Ed. Engl. *59*, 5902–5949.

18. Wang, H.Q., Wang, R.H., Song, Z.H., Zhang, H.M., Zhang, H.Z., Wang, Y.G., and Li, X.F. (2019). A novel aqueous Li^+ (or Na^+)/Br^- hybrid-ion battery with super high areal capacity and energy density. J. Mater. Chem. A Mater. Energy Sustain. *7*, 13050–13059.

19. Jameson, A., and Gyenge, E. (2020). Halogens as positive electrode active species for flow batteries and regenerative fuel cells. Electrochem. Energy Rev. *3*, 431–465.

20. Huskinson, B., Marshak, M.P., Suh, C., Er, S., Gerhardt, M.R., Galvin, C.J., Chen, X., Aspuru-Guzik, A., Gordon, R.G., and Aziz, M.J. (2014). A metal-free organic-inorganic aqueous flow battery. Nature *505*, 195–198.

21. Weng, G.M., Li, Z.J., Cong, G.T., Zhou, Y.C., and Lu, Y.C. (2017). Unlocking the capacity if iodide for high-energy-density zinc/ polyiodide and lithium/ polyiodide redox flow batteries. Energy Environ. Sci. *10*, 735–741.

22. Chen, H., Zou, Q., Liang, Z., Liu, H., Li, Q., and Lu, Y.C. (2015). Sulphur-impregnated flow cathode to enable high-energy-density lithium flow batteries. Nat. Commun. *6*, 5877.

23. Zhao, Y., Ding, Y., Song, J., Peng, L.L., Goodenough, J.B., and Yu, G.H. (2014). A reversible Br_2/Br^- redox couple in the aqueous phase as a high-performance catholyte for alkali-ion batteries. Energy Environ. Sci. *7*, 1990–1995.

24. Lee, J.H., Byun, Y., Jeong, G.H., Choi, C., Kwen, J., Kim, R., Kim, I.H., Kim, S.O., and Kim, H.T. (2019). High-energy efficiency membraneless flowless Zn-Br battery: utilizing the electrochemical-chemical growth of polybromides. Adv. Mater. *31*, e1904524.

25. Suresh, S., Ulaganathan, M., and Pitchai, R. (2019). Realizing highly efficient energy retention of Zn-Br_2 redox flow battery using rGO supported 3D carbon network as a superior electrode. J. Power Sources *438*, 226998.

26. Naresh, R.P., Mariyappan, K., Archana, K.S., Suresh, S., Ditty, D., Ulaganathan, M., and Ragupathy, P. (2019). Activated carbon-anchored 3D carbon network for bromine activity and its enhanced electrochemical performance in Zn- Br_2 hybrid redox flow battery. ChemElectroChem *6*, 5688–5697.

27. Wang, C.H., Lai, Q.Z., Xu, P.C., Zheng, D.Y., Li, X.F., and Zhang, H.M. (2017). Cage-like porous carbon with superhigh activity and Br_2-complex-entrapping capability for bromine-based flow batteries. Adv. Mater. *29*, 1605815.

28. Wu, M.C., Zhao, T.S., Zhang, R.H., Wei, L., and Jiang, H.R. (2018). Carbonized tubular polypyrrole with a high activity for the Br_2/Br^- redox reaction in zinc-bromine flow batteries. Electrochim. Acta *284*, 569–576.

29. Wu, M.C., Jiang, H.R., Zhang, R.H., Wei, L., Chan, K.Y., and Zhao, T.S. (2019). N-doped graphene nanoplatelets as a highly active catalyst for Br_2/Br^- redox reactions in zinc-bromine flow batteries. Electrochim. Acta *318*, 69–75.

30. Jin, C.X., Lei, H.Y., Liu, M.Y., Tan, A.D., Piao, J.H., Fu, Z.Y., Liang, Z.X., and Wang, H.H. (2020). Low-dimensional nitrogen-doped carbon for Br_2/Br^- redox reaction in zinc-bromine flow battery. Chem. Eng. J. *380*, 122606.

31. Xiang, H.X., Tan, A.D., Piao, J.H., Fu, Z.Y., and Liang, Z.X. (2019). Efficient nitrogen-doped carbon for zinc-bromine flow battery. Small *15*, e1901848.

32. Liu, S.M., Liang, Y.R., Zhou, W., Hu, W.Q., Dong, H.W., Zheng, M.T., Hu, H., Lei, B.F., Xiao, Y., and Liu, Y.L. (2018). Large-scale synthesis of porous carbon via one-step $CuCl_2$ activation of rape pollen for high performance supercapacitors. J. Mater. Chem. A Mater. Energy Sustain. *6*, 12046–12055.

33. Wang, Y.F., Chen, B.W., Zhang, Y., Fu, L.J., Zhu, Y., Zhang, L.X., and Wu, Y.P. (2016). ZIF-8@MWCNT-derived carbon composite as electrode of high performance for supercapacitor. Electrochim. Acta *213*, 260–269.

34. Takagi, H., Maruyama, K., Yoshizawa, N., Yamada, Y., and Sata, Y. (2004). XRD analysis of carbon stacking structure in coal during heat treatment. Fuel *83*, 2427–2433.

35. Zhang, K., Zhang, L.L., Zhao, X.S., and Wu, J.S. (2010). Graphene/ polyaniline nanofiber composites as supercapacitor electrodes. Chem. Mater. *22*, 1392–1401.

36. Baibarac, M., Baltog, I., Godon, C., Lefrant, S., and Chauvet, O. (2004). Covalent functionalization of single-walled carbon nanotubes by aniline electrochemical polymerization. Carbon *42*, 3143–3152.

37. Cong, H.P., Ren, X.C., Wang, P., and Yu, S.H. (2013). Flexible graphene-polyaniline composite paper for high-performance supercapacitor. Energy Environ. Sci. *6*, 1185–1191.

38. Petrov, M.M., Konev, D.V., Kuznetsov, V.V., Antipov, A.E., Glazkov, A.T., and Vorotyntsev, M.A. (2019). Electrochemically driven evolution of Br-containing aqueous solution composition. J. Electroanal. Chem. (Lausanne) *836*, 125–133.

39. Wu, M.C., Zhao, T.S., Wei, L., Jiang, H.R., and Zhang, R.H. (2018). Improved electrolyte for zinc-bromine flow batteries. J. Power Sources *384*, 232–239.

40. Simon, P., and Gogotsi, Y. (2008). Materials for electrochemical capacitors. Nat. Mater. *7*, 845–854.

41. Angelopoulos, M., Ray, A., and Macdiarmid, A.G. (1987). Polyaniline: processability from aqueous solutions and effect of water vapor on conductivity. Synth. Met. *21*, 21–30.

42. Louarn, G., Lapkowski, M., Quillard, S., Pron, A., Buisson, J.P., and Lefrant, S. (1996). Vibrational properties of polyanilines-isotope effects. J. Phys. Chem. *100*, 6998–7006.

43. Boyer, M.I., Quillard, S., Louarn, G., Froyer, G., and Lefrant, S. (2000). Vibrational study of the $FeCl_3$-doped dimer of polyaniline: a good model compound of emeraldine salt. J. Phys. Chem. B *104*, 8952–8961.

44. Augustyn, V., Come, J., Lowe, M.A., Kim, J.W., Taberna, P.L., Tolbert, S.H., Abruña, H.D., Simon, P., and Dunn, B. (2013). High-rate electrochemical energy storage through Li^+ intercalation pseudocapacitance. Nat. Mater. *12*, 518–522.

45. Rubinstein, I. (1981). Electrode kinetics of the Br_2/Br couple. J. Phys. Chem. *85*, 1899–1906.

46. Mastragostino, M., and Gramellini, C. (1985). Kinetic study of the electrochemical processes of the bromine/bromide aqueous system on vitreous carbon electrodes. Electrochim. Acta *30*, 373–380.

47. Wang, C.H., Lai, Q.Z., Feng, K., Xu, P.C., Li, X.F., and Zhang, H.M. (2018). From zeolite-type metal organic framework to porous nano-sheet carbon: High activity positive electrode material for bromine-based flow batteries. Nano Energy *44*, 240–247.

48. Grzeszczuk, M., and Szostak, R. (2003). Electrochemical and Raman studies on the redox switching hysteresis of polyaniline. Solid State Ion. *157*, 257–262.

49. Ohira, M., Sakai, T., Takeuchi, M., Kobayashi, Y., and Tsuji, M. (1987). Raman and infrared spectra of polyaniline. Synth. Met. *18*, 347–352.

50. Trchová, M., Morávková, Z., Bláha, M., and Stejskal, J. (2014). Raman spectroscopy of polyaniline and oligoaniline thin films. Electrochim. Acta *122*, 28–38.

51. do Nascimento, G.M., Kobata, P.Y.G., and Temperini, M.L.A. (2008). Structural and vibrational characterization of polyaniline nanofibers prepared from interfacial polymerization. J. Phys. Chem. B *112*, 11551–11557.

52. Ćirić-Marjanović, G., Trchová, M., and Stejskal, J. (2008). The chemical oxidative polymerization of aniline in water: Raman spectroscopy. J. Raman Spectrosc. *39*, 1375–1387.

53. Cochet, M., Louarn, G., Quillard, S., Buisson, J.P., and Lefrant, S. (2000). Theoretical and experimental vibrational study of emeraldine in salt form. Part II. J. Raman Spectrosc. *31*, 1041–1049.

54. Lu, Y., and Chen, J. (2020). Prospects of organic electrode materials for practical lithium batteries. Nat. Rev. Chem. *4*, 127–142.

55. Frisch, M.J., Trucks, G.W., Schlegel, H.B., Scuseria, G.E., Robb, M.A., Cheeseman, J.R., Scalmani, G., Barone, V., Mennucci, B., Petersson, G.A., et al. (2016). Gaussian 16, Revision C.01 (Gaussian, Inc.).